Controlling multimode coupling by boundary-wave scattering

Li Ge,[1,2,*] Qinghai Song,[3] Brandon Redding,[4] Alexander Eberspächer,[5] Jan Wiersig,[5] and Hui Cao[4,†]

[1]*Department of Engineering Science and Physics, College of Staten Island, CUNY, Staten Island, New York 10314, USA*

[2]*Department of Electrical Engineering, Princeton University, Princeton, New Jersey 08544, USA*

[3]*Department of Electronic and Information Engineering, Shenzhen Graduate School, Harbin Institute of Technology, Shenzhen 518055, China*

[4]*Department of Applied Physics, Yale University, New Haven, Connecticut 06520-8482, USA*

[5]*Institut für Theoretische Physik, Universität Magdeburg, Postfach 4120, D-39016 Magdeburg, Germany*

(Received 24 May 2013; published 2 October 2013)

We show that coupling among multiple resonances can be conveniently introduced and controlled by boundary wave scattering. This is demonstrated in optical microcavities of quasicircular shapes, where the couplings of multiple modes are determined by the scattering from harmonic boundary deformations. We analyze these couplings using a perturbation theory, which gives an intuitive understanding of the lowest-order and higher-order scattering processes. Different scattering paths between two boundary waves can either enhance or reduce their coupling strength. The effect of controlled multimode coupling is most pronounced in the direction of output from an open cavity, as the coupling can cause a dramatic change of the external cavity field distribution.

DOI: 10.1103/PhysRevA.88.043801 PACS number(s): 42.25.Gy, 42.55.Sa, 03.65.Nk

I. INTRODUCTION

Eigenmodes are fundamental in understanding all quantum and wave phenomena. Take optical microcavities [1,2], for example; the study of their eigenmodes has attracted considerable interest in the pursuit of compact coherent light sources [3–5], understanding quantum chaos in open systems [6,7], and achieving strong light-matter interactions [8,9]. For microdisk lasers in particular, one focus has been optimizing their output directionality while maintaining a high quality (Q) factor. One approach is deforming the circular cavity boundary [6,7,10–12], which alters the dynamics of light trapped inside the cavity. Its effect is depicted by the ray model for cavities much larger than the laser wavelength, which, however, does not apply to the cavities of the wavelength scale [13,14]; in this regime the output directions of high-Q modes in a given cavity are no longer universal or determined by the intracavity ray dynamics. Instead, mode coupling plays an important role, as found in previous studies, and it is important to understand it beyond the usual phenomenological model [15].

Mode coupling in general occurs when the orthogonality or biorthogonality in the system is modified, which can be introduced, for example, by matter-mediated interaction in cavity quantum electrodynamics [16], by nonlinearity in multimode lasers [17], and by linear scattering from a local defect or a gradual boundary deformation in waveguides [18] and microcavities [19,20]. In the latter scenario, several of the authors recently found that a minute boundary deformation can lead to a drastic change of the outcoupling direction in an open system, which was attributed to enhanced two-mode coupling caused by quasidegeneracy in the unperturbed eigenmode spectrum [21].

In this paper we show that *multimode* coupling can be achieved and controlled by boundary wave scattering. This applies to the general eigenvalue problem

$$[-\nabla^2 + V(\vec{r})]\psi(\vec{r}) = E\psi(\vec{r}), \tag{1}$$

which can be realized, for example, in a dielectric microcavity [1,2], a vibrating membrane [22], an optical trap for exciton-polariton condensate [23], and a quantum dot [24]. The scalar eigenmodes $\psi(\vec{r})$ represent vibrational amplitudes, field components of the electromagnetic waves, or probability wave functions in the corresponding physical systems.

Below we exemplify the properties of boundary wave scattering in open quasicircular cavities, with $V(\vec{r}) = -(n^2 - 1)E$ inside and $V(\vec{r}) = 0$ outside. Equation (1) then becomes the scalar two-dimensional Helmholtz equation, which describes, for example, the propagation of transverse-electric (TE) or transverse-magnetic (TM) waves in a dielectric microdisk cavity of refractive index n. For simplicity, we assume the cavity shape is nearly circular and symmetric along the horizontal axis $\theta = 0^\circ, 180^\circ$, and we describe the cavity boundary using harmonic series

$$\rho(\theta) \equiv R\left[1 + \sum_{\nu} \varepsilon_\nu \cos(\nu\theta)\right] \quad (\nu = 2,3,\ldots), \tag{2}$$

where R is the average radius of the cavity. The dipolar term ($\varepsilon_1 \cos\theta$) is not included because it mostly leads to a lateral shift of the cavity if $|\varepsilon_1| \ll 1$ and can be eliminated by choosing a proper origin. The harmonic boundary deformations in (2) can be employed as individual turning knobs to introduce and control couplings among multiple modes of different angular momenta, which is a generalization of the procedure introduced in Ref. [21]. Such a scheme can be utilized to alter the outcoupling direction of an eigenmode deterministically, through first-order and higher-order boundary wave scattering.

This paper is organized as follows. In Sec. II we review the perturbation theory for the scalar Helmholtz equation in a quasicircular cavity. We relate each perturbation contribution in the presence of the harmonic deformations in (2) to scattering strengths of different orders. In Sec. III we demonstrate multimode coupling via a *single* harmonic boundary deformation using TM modes. In Sec. IV we examine how *multiple* harmonic boundary deformations can be introduced to control couplings among TM modes. In Sec. V we apply this

*li.ge@csi.cuny.edu
†hui.cao@yale.edu

technique to control the emission directionality of microdisk lasers. The summary is given in Sec. VI.

II. PERTURBATION THEORY

We begin by reviewing the perturbation theory for TM [25,26] and TE modes [21] of the scalar Helmholtz equation in a quasicircular system. In the absence of deformation, each eigenmode φ of the circular system is characterized by its angular momentum m and radial quantum number η. The latter indicates the number of intensity peaks in the radial direction inside the cavity, and we will refer to the modes with $\eta \ll m$ as the boundary waves since they are confined closely to the inside of the cavity boundary. For convenience, we represent their angular dependence by sine and cosine functions, i.e.,

$$\varphi_{m,\eta}(\vec{r}) \propto \begin{cases} J_m(nK_{m,\eta}r)\cos(m\theta), \\ J_m(nK_{m,\eta}r)\sin(m\theta), \end{cases} \tag{3}$$

inside the cavity, where $K_{m,\eta}$ is the complex resonant frequency, corresponding to the square root of E in Eq. (1). Outside the cavity $\varphi_{m,\eta}(\vec{r})$ are similarly defined, with the Bessel functions $J_m(nK_{m,\eta}r)$ replaced by the Hankel functions of the first kind $H_m(K_{m,\eta}r)$ and properly normalized to guarantee the continuity of $\varphi_{m,\eta}(\vec{r})$ at the cavity boundary. The value of $K_{m,\eta}$ is determined by the boundary condition

$$S_m(Z) \equiv n\frac{J'_m(nZ)}{J_m(nZ)} - \frac{H'_m(Z)}{H_m(Z)} = 0 \tag{4}$$

for TM modes and

$$T_m(Z) \equiv \frac{1}{n}\frac{J'_m(nZ)}{J_m(nZ)} - \frac{H'_m(Z)}{H_m(Z)} = 0 \tag{5}$$

for TE modes, where $Z \equiv KR$.

The eigenmodes inside the cavity are slightly perturbed in the presence of a minute boundary deformation. The perturbed modes each have a dominant angular momentum m and recognizable radial quantum number η, and they are still parity eigenstates about the horizontal symmetry axis if the boundary takes the form of Eq. (2). We denote them as $\psi_{m,\eta}$ and their resonant frequencies as $k_{m,\eta}$ to distinguish them from the unperturbed modes $\varphi_{m,\eta}$ and their frequencies $K_{m,\eta}$. Below we focus on the even-parity modes, and the analysis for the odd-parity modes is similar. We drop the indices of ψ, φ, k, and K unless they are important. Using the ansatz

$$\psi(\vec{r}) = \begin{cases} \sum_{p\geqslant 0} a_p \frac{J_p(nkr)}{J_p(nkR)}\cos(p\theta), & r < \rho(\theta), \\ \sum_{p\geqslant 0}(a_p + b_p)\frac{H_p(kr)}{H_p(kR)}\cos(p\theta), & r > \rho(\theta), \end{cases} \tag{6}$$

and $a_m \equiv 1$ for the dominant angular momentum, Dubertrand *et al*. found that in a cavity with the boundary given by

$$\rho(\theta) = R[1 + \varepsilon f(\theta)], \quad f(\theta) = f(-\theta), \tag{7}$$

the perturbed quantities are

$$kR = Z\left[1 - \varepsilon A_{mm} - \varepsilon^2\left(Z(n^2-1)\sum_{q\neq m} A_{mq}A_{qm}\frac{1}{S_q} - \frac{3A_{mm}^2 - B_{mm}}{2} - Z\left(A_{mm}^2 - B_{mm}\right)\frac{H'_m}{H_m}\right)\right], \tag{8}$$

$$a_p = \varepsilon Z(n^2-1)\frac{1}{S_p}\left(A_{pm} + \varepsilon\left\{A_{pm}A_{mm}\left(\frac{Z}{S_p}S'_p - 1\right) + \frac{B_{pm}}{2}\left[1 + Z\left(\frac{H'_m}{H_m} + \frac{H'_p}{H_p}\right)\right] + Z(n^2-1)\sum_{q\neq m} A_{pq}A_{qm}\frac{1}{S_q}\right\}\right), \tag{9}$$

$$b_p = \frac{\varepsilon^2 Z^2}{2}(n^2-1)B_{pm} \tag{10}$$

up to order $O(\varepsilon^2)$ for TM modes [25]. We have dropped the argument Z in S, H, and their derivatives S', H' with respect to Z. The coefficients A_{pm}, B_{pm} are given by

$$A_{pm} \equiv \frac{c_p}{\pi}\int_0^\pi f(\theta)\cos(p\theta)\cos(m\theta)d\theta, \tag{11}$$

$$B_{pm} \equiv \frac{c_p}{\pi}\int_0^\pi f^2(\theta)\cos(p\theta)\cos(m\theta)d\theta, \tag{12}$$

with $c_p = 2(p > 0), 1(p = 0)$.

The perturbation theory was extended to TE modes in Ref. [21], which is more complicated due to the discontinuity of the radial derivative of ψ at the cavity boundary. The results up to the order $O(\varepsilon)$ are given by

$$kR = Z[1 - \varepsilon A_{mm}], \tag{13}$$

$$a_p = \varepsilon Z\left[S_m\left(\frac{H'_p}{H_p} - \frac{H'_m}{H_m}\right) - T'_m\right]\frac{1}{T_p}A_{pm}, \tag{14}$$

$$b_p = \varepsilon Z S_m A_{pm}, \tag{15}$$

and we note that b_p now has a first-order term in ε and kR has the same expression for TE and TM modes to the first order.

The creation of angular momentum sidebands $a_{p\neq m}$ inside the cavity can be considered the result of boundary wave scattering. The perturbation results above give an intuitive understanding of these scattering processes. Take the TM polarization as an example; a_p given by Eq. (9) can be rearranged as

$$a_p = \alpha_{pm} + \sum_{q\neq m}\alpha_{pq}\alpha_{qm} + (\cdots)B_{pm} + (\cdots)A_{pm}A_{mm}, \tag{16}$$

where

$$\alpha_{pm} = \varepsilon Z(n^2-1)\frac{1}{S_p}A_{pm} \tag{17}$$

can be considered the scattering strength for the first-order process $m \to p$ by the $\cos(m \pm p)\theta$ deformation in (2). In our notation the angular momenta m, p of the boundary waves are non-negative, representing the clockwise (CW) wave with a positive sign and counterclockwise (CCW) wave with a negative sign. For example, the $\cos(m - p)\theta$ deformation can scatter the CW (CCW) wave of angular momentum m $(-m)$ into the CW (CCW) wave of angular momentum p $(-p)$, and the $\cos(m + p)\theta$ deformation can scatter the CW (CCW) wave of angular momentum m $(-m)$ into the CCW (CW) wave of angular momentum p $(-p)$.

We emphasize that the scattering strength α_{pm} is mode dependent; it is proportional to $S_p^{-1}(K_{m,\eta}R)$, which we will refer as the spectral function. If there is another resonance

$K_{p,\eta'}$ in the vicinity of $K_{m,\eta}$, we then find $S_p(K_{m,\eta}R) \approx S_p(K_{p,\eta'}R) = 0$, and the scattering from m to p in mode $\psi_{m,\eta}$ is enhanced [21]. The scattering from p to m in mode $\psi_{p,\eta'}$ is also enhanced. η' is the radial quantum number of the second mode, which is typically different from η for two quasidegenerate modes. In the Appendix we show that for high-Q modes of $\eta = 1$, this sensitivity due to a low-order harmonic boundary deformation maximizes in the mesoscopic regime that lies in the crossover between the microscopic regime ($\lambda \sim R$) and the macroscopic regime (semiclassical limit $\lambda \ll R$), where λ is the wavelength.

The second term in Eq. (16) represents different paths that consist of two successive first-order scattering processes, i.e., $m \to q \to p$ for all $q \neq m$. Such second-order processes depend not only on the spectral function of the final state [i.e., $S_p^{-1}(K_{m,\eta}R)$] but also on the spectral function of the intermediate state [i.e., $S_q^{-1}(K_{m,\eta}R)$]. There is another type of second-order processes in a_p, which is represented by the term proportional to B_{pm} in Eqs. (9) and (16). Their scattering strengths do not depend on the spectral function of the intermediate state; thus we will refer to them as "virtual" processes. The last $O(\varepsilon^2)$ term in Eq. (16) has a more complicated dependence on the spectral function of the final state. Its scattering strength is proportional to A_{mm}, which represents the scattering of the CW and CCW waves of angular momentum $\pm m$ into each other by the $\cos(2m\theta)$ deformation.

III. MULTIMODE COUPLING VIA A SINGLE HARMONIC BOUNDARY DEFORMATION

In this section and the next section we exemplify multimode coupling using the TM polarized modes. Let us first consider a single harmonic perturbation $\cos(\nu\theta)$ with an amplitude $|\varepsilon_\nu| \ll 1$. As we have discussed in the previous section, this boundary deformation scatters the boundary wave of angular momentum m into two sidebands $m \pm \nu$ to the leading order, whose amplitudes are given by

$$\alpha_{m\pm\nu,m} = \frac{\varepsilon_\nu(n^2-1)Z}{2S_{m\pm\nu}} \tag{18}$$

from Eq. (17). This boundary wave scattering introduces coupling between $\varphi_{m,\eta}$ and two other modes, $\varphi_{m+\nu,\eta'}$ and $\varphi_{m-\nu,\eta''}$, whose dominant angular momenta are $m+\nu$ and $m-\nu$, respectively.

Higher-order scattering processes create weaker sidebands at $m \pm 2\nu, m \pm 3\nu, \ldots$, coupling more modes with decreasing strength in general. The strength $\beta_{m\pm2\nu,m}$ of the second-order scattering can be found in Eq. (16):

$$\beta_{m\pm2\nu,m} \approx \alpha_{m\pm2\nu,m\pm\nu}\alpha_{m\pm\nu,m}. \tag{19}$$

We have assumed $\nu < m$, with which A_{mm} and the last term in Eq. (16) vanish. We have also neglected the "virtual" process given by B_{pm} in Eq. (16); it is weak compared with the right-hand side of Eq. (19) since it does not depend on the spectral function $S_{m\pm\nu}^{-1}$ of the intermediate state, which needs to be large for the second-order scattering strength to be non-negligible.

In Fig. 1 we show one example with a $\cos(3\theta)$ boundary deformation in a circular cavity of index $n = 3.13$. Near $KR = 4.6$ there are three eigenmodes of angular momenta $m = 11, m' = 8, m'' = 5$ and radial quantum numbers $\eta = 1$, $\eta' = 2$, $\eta'' = 3$. They are calculated using a scattering-matrix method similar to that described in Refs. [10,27]. We refer to them as modes 1, 1′, and 1″, and they have increasing cavity decay rates, defined by $\kappa = -2\mathrm{Im}[KR] > 0$. We first focus on mode 1 ($m = 11$) and point out that the two first-order sidebands of mode 1 at $p = 8, 14$ do not have equal strength; the presence of mode 1′ ($m' = 8$) leads to a spectral function $S_8^{-1} > S_{14}^{-1}$, and the sideband at $p = 8$ is about four times stronger than that at $p = 14$. Similarly, the proximity of mode 1″ ($m'' = 5$) enhances the scattering into the second-order sideband of mode 1 at $p = 5$, which is even stronger than the first-order one at $p = 14$.

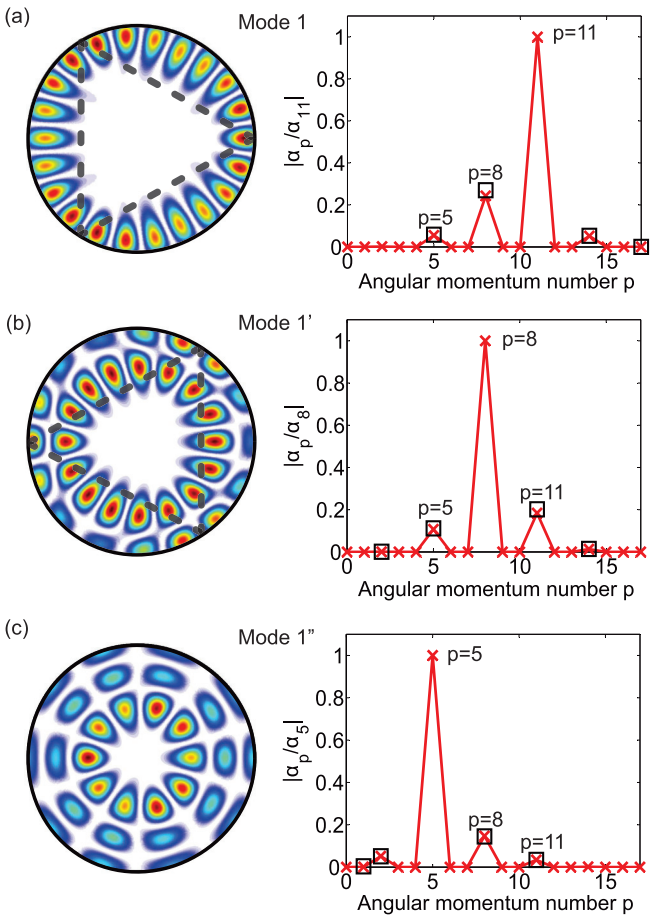

FIG. 1. (Color online) Mutual coupling of three TM modes in a quasicircular cavity $\rho(\theta) \equiv R[1 + 0.01\cos(3\theta)]$. (a) Intracavity intensity distribution (left) and angular momentum components $|a_p|$ (right) of mode 1 at $k_{11,1}R = 4.593 - 1.603 \times 10^{-4}i$. Connected crosses show the numerical values of $|\alpha_p|$, and black squares show the perturbation results from Eqs. (18) and (19). (b) and (c) Same as (a) for two nearby modes at $k_{8,2}R = 4.699 - 1.351 \times 10^{-3}i$ (mode 1′) and $k_{5,3}R = 4.515 - 4.046 \times 10^{-2}i$ (mode 1″). The dominant angular momenta for modes 1, 1′, and 1″ are 11, 8, and 5, respectively. Mode 1 (1′) has enhanced intensity near a triangular orbit $\triangleright$ ($\triangleleft$), which is marked by the dashed line.

Figures 1(b) and 1(c) for modes 1′ and 1″ further display the mutual coupling between them and mode 1. The couplings, however, affect these eigenmodes differently. For example, their decay rates all vary on the scale of 10^{-4} when ε_3, the amplitude of the $\cos(3\theta)$ boundary deformation, changes from

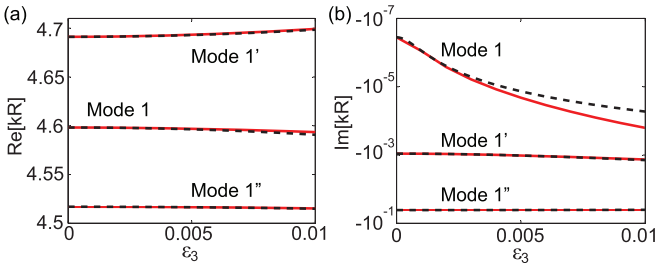

FIG. 2. (Color online) Effect of the $\cos(3\theta)$ deformation of the cavity boundary on the complex frequencies of the three modes in Fig. 1. Solid lines and black dashed lines show the numerical data and the second-order perturbation result from Eq. (20), respectively. The relative change of the decay rate of mode 1, which has the highest Q factor, is much larger than for modes $1'$ and $1''$.

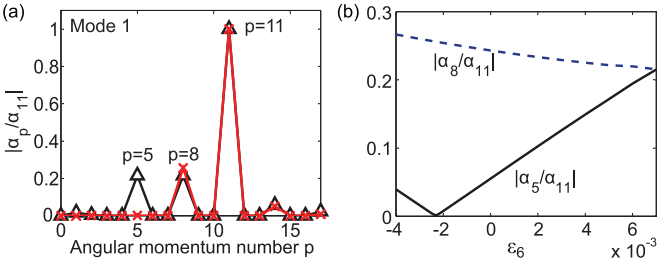

FIG. 3. (Color online) Controlling the $p = 5$ component in mode 1 using the interference of multiple scattering paths, i.e., the second-order scattering $m = 11 \to q = 8 \to p = 6$ by the $\cos(3\theta)$ deformation discussed in Fig. 1 and the first-order scattering $m = 11 \to p = 6$ by an additional $\cos(6\theta)$ deformation. (a) Angular momentum components $|\alpha_p|$ of mode 1 inside the cavity at $\varepsilon_6 = -0.0023$ (connected red crosses) and 0.006 (connected black triangles). (b) $|\alpha_5|$ and $|\alpha_8|$ of mode 1 as a function of ε_6. ε_3 is fixed at 0.01. The $p = 5$ component almost vanishes at $\varepsilon_6 = -0.0023$ and is raised to about the same height as the $p = 8$ component at $\varepsilon_6 = 0.007$.

0 to 0.01. This shift can be shown to be a quadratic function of ε_3,

$$k = K\left(1 - \frac{\alpha_{m-3,m} + \alpha_{m+3,m}}{2}\varepsilon_3\right), \tag{20}$$

where $\alpha_{m-3,m}, \alpha_{m+3,m}$ are given by Eq. (18) and are linear in ε_3. Equation (20) is derived from Eq. (8) using the fact that both A_{mm} and B_{mm} vanish in this example. Such a variation barely changes the cavity decay rates of modes $1'$ and $1''$ but increases that of mode 1 by more than two orders of magnitude [see Fig. 2(b)].

Another example of the different effects of multimode couplings on these modes is their intracavity field distribution. Close to the cavity boundary the wave function (6) inside the cavity can be approximated by

$$\psi_m(R,\theta) \approx \cos(m\theta) + \sum_{p=m\pm\nu} \alpha_{pm}\cos(p\theta), \tag{21}$$

with the higher-order sidebands neglected. The phases of α_{pm} determine the field distribution inside the cavity. For example, we find that both $\alpha_{8,11}$ and $\alpha_{14,11}$ are almost real and *positive* at a positive ε_3 from Eq. (18). We then expect both sidebands at $p = 8, 14$ in mode 1 to interfere constructively with the dominant angular component $m = 11$ at $\theta \approx 0^\circ, 120^\circ, 240^\circ$, resulting in enhanced intensity near a triangular orbit ($\triangleright$). Similarly, Eq. (18) predicts that $\alpha_{5,8}, \alpha_{11,8}$ are almost real but *negative* at a positive ε_3. The beating of the $p = 11, 5$ sidebands in mode $1'$ with the dominant $m' = 8$ component then leads to an enhanced field intensity at $\theta \approx 60^\circ, 180^\circ, 300^\circ$, leading to a triangle of opposite orientation ($\triangleleft$). These predictions are confirmed by the numerical calculations shown in Fig. 1.

IV. MULTIMODE COUPLING VIA MULTIPLE HARMONIC BOUNDARY DEFORMATIONS

The above example illustrates how the boundary wave scattering from a *single* harmonic boundary deformation couples multiple eigenmodes. The couplings of mode $1'$ to modes 1 and $1''$ are of first order and are stronger than that between modes 1 and $1''$, which is of second order. To vary the latter without affecting the former, one can introduce extra couplings by adding additional harmonic boundary deformations. For example, a $\cos(6\theta)$ deformation adds first-order coupling between modes 1 and $1''$, which can be tuned to reduce or enhance their existing coupling due to the $\cos(3\theta)$ deformation. As shown in Fig. 3, the $p = 5$ sideband in mode 1 is almost canceled completely at $\varepsilon_6 = -0.0023$ and is raised to about the same height of the $p = 8$ sideband at $\varepsilon_6 = 0.007$. All other angular components only have a minute change with ε_6 due to higher-order scattering processes.

The tunability of the total coupling between two modes depends on the phases of individual couplings from different scattering paths. To find the general requirement that a first-order scattering $m \to p$ cancels a second-order scattering $m \to q \to p$, we again turn to Eq. (16) and employ the same approximation used in deriving Eq. (19), which leads to

$$a_p \approx \alpha_{pm} + \alpha_{pq}\alpha_{qm}. \tag{22}$$

From Eqs. (9) and (18) we know that α_{pm} and α_{pq} above are proportional to the same spectral function of the final state, i.e., S_p^{-1}. α_{pm} and α_{pq} are then in phase (π out of phase) if the amplitudes ε_{m-p} and ε_{q-p} of the harmonic modulations $\cos(m-p)\theta$ and $\cos(q-p)\theta$ have the same sign (opposite signs). Therefore the requirement for the aforementioned cancellation at some value of ε_{m-p} is to have a real α_{qm}. Indeed, we find $\mathrm{Arg}[\alpha_{8,11}] = 0.008$ in the example given above, where $m = 11$, $q = 8$, and $p = 5$, and a negative $\varepsilon_6 = -0.0023$ is needed to cancel the $p = 5$ sideband at a positive $\varepsilon_3 = 0.01$. We also note that the phase of a_p changes by about π across $\varepsilon_6 = -0.0023$ as a result.

The effect of controlled multimode coupling is most pronounced in the outcoupling of the high-Q modes. Recent studies [13,19] show that the output direction of a high-Q mode can be completely overwhelmed by that of a lower-Q mode to which it couples. The situation becomes more interesting if the high-Q mode couples to more than one lower-Q mode, such as the case in Fig. 1. Unlike the intracavity intensity distribution, which is largely determined by the dominant angular momentum and the strong first-order sidebands [see Eq. (21) and its discussion], the weaker sidebands of lower angular momenta can also have a strong influence on the outcoupling due to their stronger leakiness. More specifically,

the wave function (6) in the far field becomes

$$\psi(r \to \infty) \propto \sum_p (a_p + b_p) \frac{e^{-ip\pi/2}}{H_p(kR)} \cos(p\theta) \equiv \sum_p W_p \cos(p\theta), \quad (23)$$

using the large-argument asymptotic form of the Hankel function of the first kind

$$H_p(z \to \infty) \to \sqrt{\frac{2}{\pi z}} e^{i(z - p\pi/2 - \pi/4)}. \quad (24)$$

We note that the amplitude of $H_p(kR)$ in the denominator of Eq. (23), evaluated at the average radius of the cavity, reduces dramatically for a smaller angular momentum p, which represents the stronger leakiness mentioned above.

Now let us examine how the outcoupling direction of mode 1 changes with ε_6 in the example shown in Fig. 3. At $\varepsilon_6 = -0.0023$ the $p = 5$ sideband outside the cavity is very small, similar to what happens inside the cavity. The outcoupling of mode 1 is then dominated by the $p = 8$ sideband, which leads to an approximate angular dependence of $\cos(16\theta)$ for the far-field intensity [Fig. 4(a)]. As ε_6 changes from -0.0023, the cancellation of the two scattering paths is removed, and the coupling between modes 1 and $1''$ increases rapidly; the

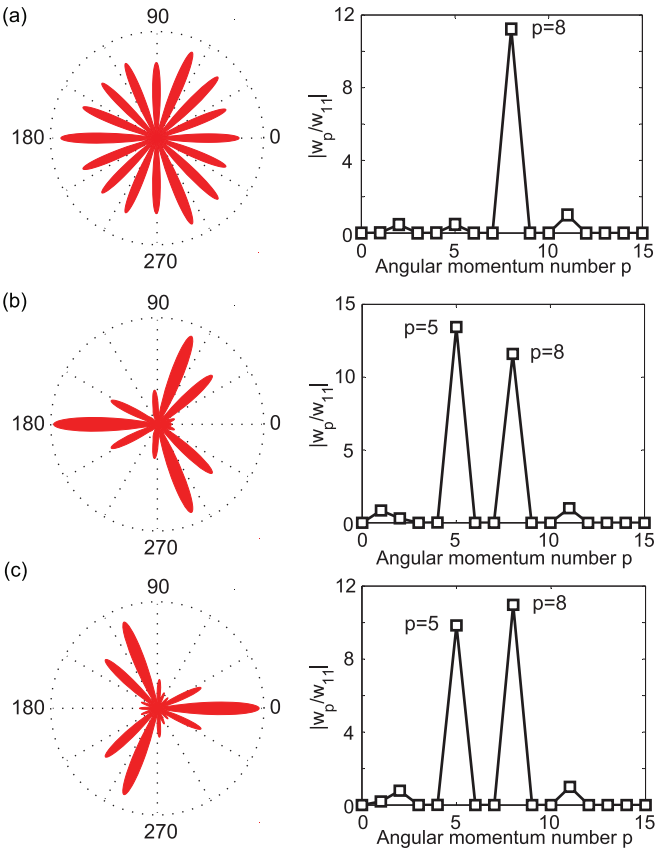

FIG. 4. (Color online) Far-field intensity pattern (left column) of mode 1 at $\varepsilon_6 = -0.0023$, -0.004, -0.001 in (a), (b), and (c), respectively. The angular components of mode 1 are shown in the right column. ε_3 is fixed at 0.01. The output directionality changes dramatically by varying the $p = 5$ component as discussed in Fig. 3.

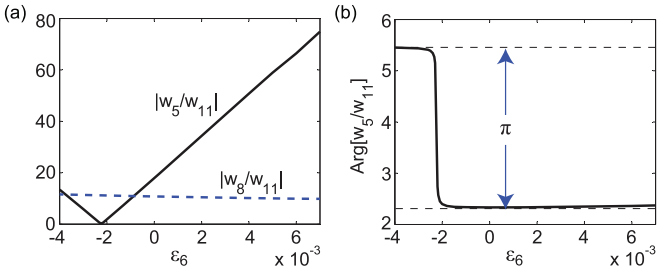

FIG. 5. (Color online) Analysis of the far-field change shown in Fig. 4. (a) Angular components $|W_5|$ and $|W_8|$ for the $\cos(5\theta)$ and $\cos(8\theta)$ terms of mode 1 outside the cavity as a function of ε_6. (b) π-phase jump of W_5 near $\varepsilon_6 = -0.0023$. The two dashed lines are separated by π and are used as references. The far-field pattern of mode 1 is determined mostly by the interference of the W_5 and W_8 terms. The strong variation of the magnitude of W_5 with ε_6 and the phase jump result in a dramatic change of the far-field pattern in Fig. 4.

$p = 5$ sideband outside the cavity becomes comparable to the $p = 8$ sideband at $\varepsilon_6 \approx -0.004, -0.001$ [see Fig. 5(a)], which are about ten times larger than the $m = 11$ component, the dominant one inside the cavity. Depending on the relative phase and amplitude of W_5 and W_8 in Eq. (23), the beating of these two largest angular components can lead to a quite different outcoupling direction. For example, using Eqs. (9) and (10), we find that W_5 and W_8 are approximately π out of phase at $\varepsilon_6 \approx -0.004$, and the outcoupling is enhanced in the $\theta \approx 60^\circ, 180^\circ, 300^\circ$ directions [Fig. 4(b)]. At $\varepsilon_6 \approx -0.001$, however, the phase of W_5 changes roughly by π [see Fig. 5(b)]. This is because W_5 is approximately proportional to a_5 since $|a_5| \gg |b_5|$ in expression (23) for the far field, and we know from our discussion of Eq. (22) that the phase of a_5 jumps by about π across $\varepsilon_6 = -0.0023$. Meanwhile, W_8 varies little for such a small change of the minute ε_6 since it depends on ε_6 only through a second-order scattering path $11 \to 5 \to 8$. As a result, W_5 and W_8 are now approximately in phase, and the outcoupling is enhanced in the $\theta \approx 0^\circ, 120^\circ, 240^\circ$ directions instead [Fig. 4(c)], which is flipped vertically from that at $\varepsilon_6 \approx -0.004$. In this process the intracavity intensity distribution of mode 1 barely changes from the $\triangleright$ pattern shown in Fig. 1(a) since the modified $p = 5$ sideband inside the cavity is very weak [see Fig. 3(b)]. Thus the flipping of the outcoupling direction with ε_6 is different from that reported in Ref. [21], which involves the flipping of the intracavity field pattern as well. As ε_6 moves farther away from -0.0023, the $p = 5$ sideband in mode 1 gradually becomes the dominant angular momentum outside the cavity [Fig. 5(a)], and the angular dependence of the outcoupling approaches $\cos(10\theta)$ (not shown).

V. CONTROL OF MICROCAVITY EMISSION PATTERN VIA MULTIMODE COUPLING

To demonstrate potential applications of the presented theory, we will show in this section that the boundary wave scattering can be used to control the directions of microcavity emission. Previously, we fabricated semiconductor microcavities of various shapes and obtained directional emissions [13,14]. Since the laser emission is predominantly

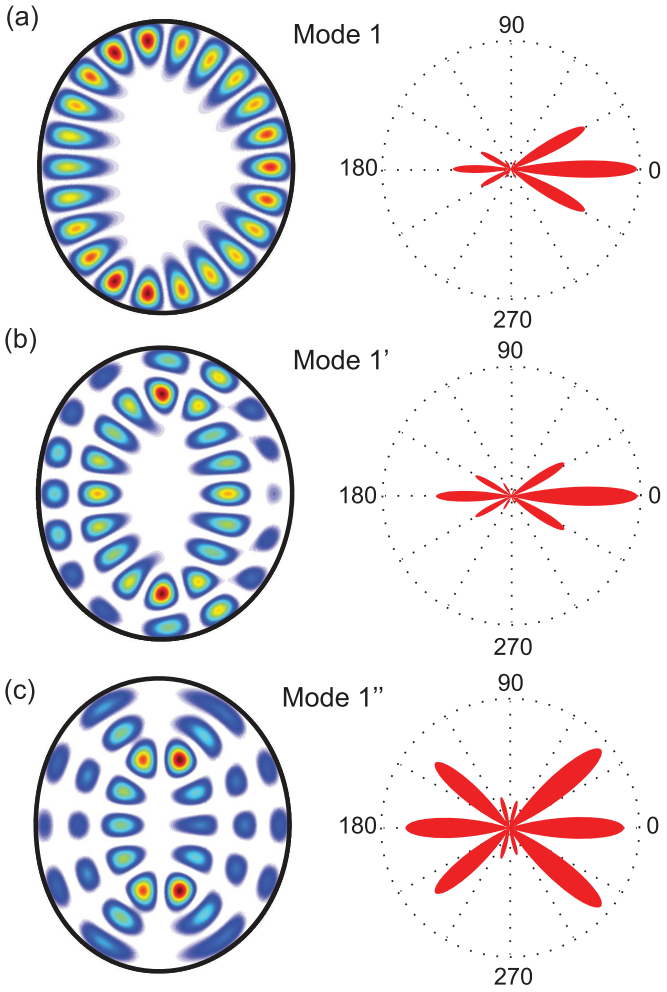

FIG. 6. (Color online) Mutual coupling of three TE modes in a quasicircular cavity with $\varepsilon_2 = -0.07$ and $\varepsilon_3 = 0.008$. (a) Intracavity intensity distribution (left) and far-field intensity pattern (right) of mode 1 at $kR = 4.895 - 7.272 \times 10^{-4}i$. (b) and (c) The same for two nearby modes at $kR = 4.991 - 2.230 \times 10^{-2}i$ (mode 1′) and $kR = 4.866 - 0.1018i$ (mode 1″).

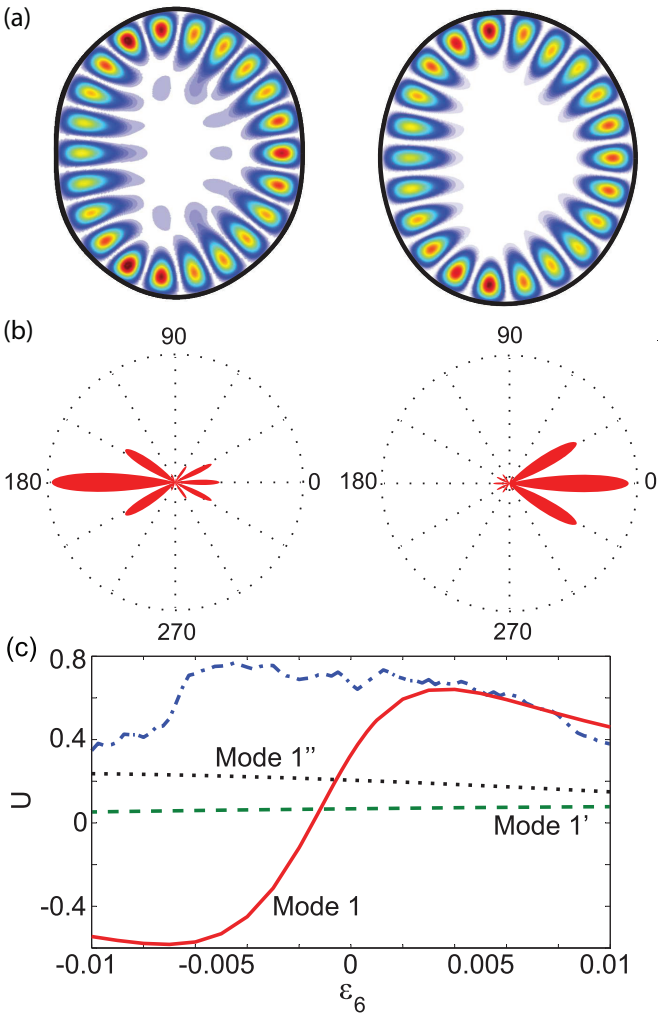

FIG. 7. (Color online) The main output direction of mode 1 in Fig. 6 is switched via the first-order scattering caused by the $\cos(6\theta)$ deformation of the cavity boundary. (a) plots its intracavity intensity distribution at $\varepsilon_6 = -0.008$ (left) and 0.004 (right). (b) shows the corresponding far-field intensity patterns. (c) plots the measure of the output directionality U for all three modes in Fig. 6 as a function of ε_6. The dash-dotted line shows the result of classical ray-tracing simulation as a comparison, which is obtained by following 50 000 initial rays uniformly distributed in the Poincaré surface of section [6,11,28] for each value of ε_6. The switching of the main output direction is not captured by the ray model, confirming that it is a wave effect.

TE polarized, we consider here the TE modes and introduce multiple harmonic terms in the boundary deformation to control the output directions.

We start with $\varepsilon_2 = -0.07$ and $\varepsilon_3 = 0.008$, and three nearby modes with $m = 11, m' = 8, m'' = 5$ can be found around $kR = 4.9$ (see Fig. 6); they are the TE correspondence of the TM modes we have discussed in Figs. 1–4, albeit the deformations are different. We find that mode 1 couples strongly to mode 1′, with similar W_p's outside the cavity. Consequently, the output directionality of mode 1 is almost identical to that of mode 1′ [Figs. 6(a) and 6(b)].

To enhance the coupling between modes 1 and 1″, we introduce a $\cos(6\theta)$ perturbation, similar to what is done in Figs. 3 and 4. We again find that the output directionality of mode 1, here indicated by

$$U \equiv \frac{\int_0^{2\pi} I(\theta)\cos\theta d\theta}{\int_0^{2\pi} I(\theta) d\theta} \tag{25}$$

to measure its "skewness" along the horizontal direction, changes dramatically from left pointing ($U < 0$) to right pointing ($U > 0$), while the output directionality of modes 1′ and 1″ barely changes [Figs. 7(b) and 7(c)]. We also perform a classical ray-tracing calculation of U for various cavity deformations; Fig. 7(c) [6,11,28] shows clearly that it does not capture the correct deformation dependence of the output directionality of mode 1, which is a wave-interference effect not taken into account in the classical ray dynamics. As shown in Fig. 7(a), the weak intensity of mode 1 near the cavity center at $\varepsilon_6 = -0.008$ is similar to that of mode 1″ in Fig. 6(c), which is already a hint that the aforementioned change of mode 1 is indeed caused by the newly introduced first-order coupling to

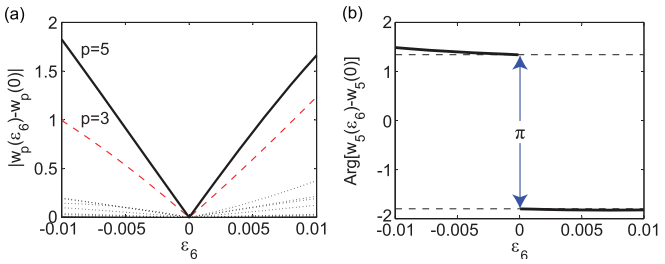

FIG. 8. (Color online) Analysis of the far-field change of mode 1 shown in Fig. 7. (a) Amplitude change of the angular components W_p in mode 1 outside the cavity as a function of ε_6. The black solid line and red dashed line represent W_5 and W_3, and low-lying dotted lines show the rest of W_p up to $p = 12$. W_6 is normalized to be 1. $|W_5(\varepsilon_6) - W_5(0)|$ indicates the strength of the first-order scattering $11 \to 5$, which varies significantly with ϵ_6. (b) Phase change of W_5 in mode 1 as a function of ε_6. It is nearly constant on both sides of $\varepsilon_6 = 0$ and jumps by π across $\varepsilon_6 = 0$. The two dashed lines are separated by π and are used as references. These results show that the switching of the output direction of mode 1 in Fig. 7 is due to the ε_6-dependent coupling to mode $1''$.

mode $1''$. To further confirm this relation, we note that the amplitudes of W_5, W_3 in mode 1 vary most noticeably and linearly with ε_6 [see Fig. 8(a)], which are exactly the two most significant components in mode $1''$ outside the cavity. In addition, the change of W_5 from its value at $\varepsilon_6 = 0$ has almost fixed phases for $\varepsilon_6 < 0$ and $\varepsilon_6 > 0$, which differ by π [Fig. 8(b)]. These observations indicate that the change of W_5 is of first order in ε_6, which is what we expect from the first-order scattering amplitude a_5 due to the $\cos(6\theta)$ deformation, given by the TE perturbation result from Eq. (14).

The coupling between modes 1 and $1''$ can also be enhanced via a second-order scattering process. By introducing a

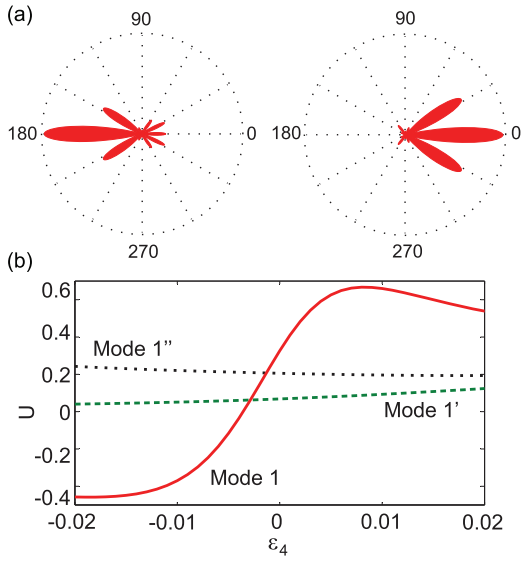

FIG. 9. (Color online) Controlling the far-field intensity pattern of mode 1 in Fig. 6 using the second-order scattering caused by the $\cos(2\theta)$ and $\cos(4\theta)$ deformations. (a) shows the switching of the main output direction from $\varepsilon_4 = -0.01$ (left) to 0.008 (right). (b) plots the measure of the output directionality U for all three modes in Fig. 6 as a function of ε_4.

$\cos(4\theta)$ boundary deformation and utilizing the large $\cos(2\theta)$ deformation, the scattering from $m = 11$ to $p = 5$ is efficiently enhanced from the two paths $11 \to 9 \to 5$ and $11 \to 7 \to 5$, while the coupling between modes 1 and $1'$ is still barely affected. As we show in Fig. 9, a similar flipping of the outcoupling direction of mode 1 is observed when ε_4 varies from -0.01 to 0.01, while those of modes $1'$ and $1''$ stay roughly the same.

VI. DISCUSSION AND CONCLUSION

Finally, we compare our study to previous works on surface scattering. Light scattering from a rough surface or inside a corrugated waveguide has been studied extensively [29–36]. For example, Ref. [33] studied the higher-order effect of longitudinal surface roughness in the direction of wave propagation in quasi-one-dimensional waveguides. Although the examples in our paper are for planar systems, the governing equation (1) is equivalent to steady-state wave propagation in quasi-two-dimensional waveguides. In this waveguide analog the surface roughness we consider is transverse instead, with no variation in the longitudinal direction of the waveguide. We also note that Ref. [33] considered a closed (i.e., Dirichlet) boundary condition in the cross section of the waveguide, while we consider an open (i.e., outgoing) boundary condition. Despite the different scattering geometries, there are some similar features in both systems. Reference [33] found the crossover of the first- and second-order terms in the longitudinal scattering mean free path, while we discuss how the first- and second-order scatterings can have comparable amplitudes and interfere destructively or constructively. A key difference lies in the physical factors that influence the relative amplitudes of these terms. One dominant factor shown in our work is the spectral overlap of adjacent resonances or quantized modes of the cross section, which is absent in Ref. [33] given that the one-dimensional cross section considered leads to an equally spaced and nonoverlapping transverse mode spectrum.

In summary, we have shown a convenient approach to achieve and control multimode coupling using boundary wave scattering. The examples given are for solutions of the scalar Helmholtz equation with two types of open boundary conditions in quasicircular systems. Fine-tuning of the harmonic boundary deformation has been demonstrated, for example, in a liquid-jet column [37], and the general principle should also apply for a wide variety of Hamiltonians in other geometries, unless the scattering is prohibited by a topological property of the material [38–40]. The boundary wave scattering presented is a linear and elastic analog of Brillouin scattering [41] in a circular geometry [42], where the angular momentum plays the roles of frequency. The boundary wave scattering can also couple modes within the cavity plane to propagating modes in the free space [43]. The cancellation of the scattering from $m = 11$ to $p = 5$ by the destructive interference of two scattering paths shown in Fig. 3 closely resembles the vanishing of absorption in electromagnetically induced transparency [44].

ACKNOWLEDGMENTS

We acknowledge A. Douglas Stone, Eugene Bogolmony, and Remy Dubertrand for helpful discussions. L.G.

acknowledges MIRTHE NSF under Grant No. EEC-0540832. Q.S. acknowledges Grant No. 2011KFB005 of the State Key Laboratory on Integrated Optoelectronics and NSFC under Grant No. 11204055. B.R. and H.C. acknowledge NSF under Grants No. ECCS-1068642 and No. ECCS-1128542. A.E. and J.W. acknowledge DFG research group 760.

APPENDIX: QUASIDEGENERACY AND THE SPECTRAL FUNCTION

In the appendix we discuss how the boundary wave scattering of high-Q modes depends on the frequency regime. We are most interested in the $\eta = 1$ modes, which have the smallest cavity decay rates and thus the lowest thresholds once optical gain is introduced to the cavity. In Ref. [21] it has been observed numerically that for these modes, the effect of boundary wave scattering from a minute low-order harmonic boundary deformation is most dramatic in the mesoscopic regime, i.e., the crossover regime between the microscopic regime ($\lambda \sim R$) and the macroscopic regime (semiclassical limit $\lambda \ll R$), where $\lambda = 2\pi/\mathrm{Re}[k]$ is the wavelength; the effect becomes very weak in the semiclassical limit. Below we point out that the key to understanding this phenomenon lies in the spectral function $S_p^{-1}(K_{m,1}R)$ for TM waves [or $T_p^{-1}(K_{m,1}R)$ for TE waves; see Eq. (14)], which in turn depends on the frequency spacing between $K_{m,1}$ and the nearest resonance of angular momentum p, as mentioned in Sec. II. We denote this distance $\Delta_{m,p}$, i.e.,

$$\Delta_{m,p} = \min|K_{m,1} - K_{p,\eta}| \ \forall\ \eta, \tag{A1}$$

and note that it is determined mostly by the real part of the high-Q resonant frequencies we are interested in, whose $|\mathrm{Im}[KR]| \ll \mathrm{Re}[KR]$. Thus $\mathrm{Re}[\Delta_{m,p}] \approx \Delta_{m,p}$ is the quantity we will focus on here.

To find the frequency dependence of $\Delta_{m,p}$, we first note that all K's of the same η form a band in the $\{m,\mathrm{Re}[KR]\}$ plane [see Fig. 10(a)]. These η bands do not cross, and the slope of the $\eta = 1$ band is well approximated by $\mathrm{Re}[KR]/m \approx 1/n$ [45]. It is straightforward to find that $\Delta_{m,p}$ is capped at about $|m-p|/n$ for a given m and p, which is the distance between $K_{m,1}$ and $K_{p,1}$. For $p > m$, this is in fact the value of $\Delta_{m,p}$ since $K_{p,\eta>1}$ are farther away from $K_{m,1}$, as can be seen in Fig. 10(a). For such a relatively large $\Delta_{m,p}$, the spectral function $S_p^{-1}(K_{m,\eta}R)$ is typically subunitary [see Fig. 10(b)], and the associated scattering processes, such as the first-order scattering $m \to p$, are very weak. For $p < m$, however, $K_{p,\eta>1}$ can be much closer to $K_{m,1}$ when compared with $K_{p,1}$, which then leads to a very large spectral function and a very strong scattering strength. To find out when this situation occurs, we employ the approximation for $\mathrm{Re}[KR]$ given in Ref. [25], which applies to both TM and TE modes of a small η:

$$\mathrm{Re}[KR] = \frac{m}{n} + \frac{\beta_\eta}{n}\left(\frac{m}{2}\right)^{1/3} - \frac{1}{\tau\sqrt{n^2-1}} + O\left(\frac{1}{m}\right)^{1/3}. \tag{A2}$$

Here $\tau = 1$ for TM modes and n^2 for TE modes, and β_η is the ηth zero of the Airy function, the first three of which are 2.34, 4.09, and 5.52. $\Delta_{m,p}$ can then be approximated by

$$\begin{aligned}\Delta_{m,p} &\approx \min\left|\frac{m-p}{n} + \frac{1}{n}\left[\beta_1\left(\frac{m}{2}\right)^{1/3} - \beta_\eta\left(\frac{p}{2}\right)^{1/3}\right]\right| \\ &= \min\left|\frac{m-p}{n} + \frac{1}{n}\left[\frac{\beta_\eta 2^{-1/3}(m-p)}{m^{2/3}+m^{1/3}p^{1/3}+p^{2/3}}\right.\right. \\ &\quad \left.\left. - (\beta_\eta - \beta_1)\left(\frac{m}{2}\right)^{1/3}\right]\right| \\ &\approx \frac{1}{n}\min\left|(m-p) - (\beta_\eta - \beta_1)\left(\frac{m}{2}\right)^{1/3}\right| \end{aligned} \tag{A3}$$

for $m - p \ll m^{2/3}$. Therefore we see that whenever

$$L \equiv \frac{m-p}{\left(\frac{m}{2}\right)^{1/3}} + \beta_1 \tag{A4}$$

approaches one $\beta_{\eta>1}$, $\Delta_{m,p}$ approaches zero, and the spectral function enhances the scattering strength. From this expression, we can then estimate the upper bound of m for this to occur at a given $\nu \equiv m - p > 0$, i.e.,

$$m_{\max} \approx 2\left[\frac{\nu}{\beta_2 - \beta_1}\right]^3 \approx 0.37\nu^3, \tag{A5}$$

which is independent of the polarization and the refractive index. For example, $m_{\max}$ from Eq. (A5) is 10 and 81 for $\nu = 3,6$, respectively, which agrees qualitatively with the numerical value of 12 and 76 shown in Fig. 10(b). For $m > m_{\max}$, the spectral function $S_{m-\nu}^{-1}(K_{m,1}R)$ tails off and

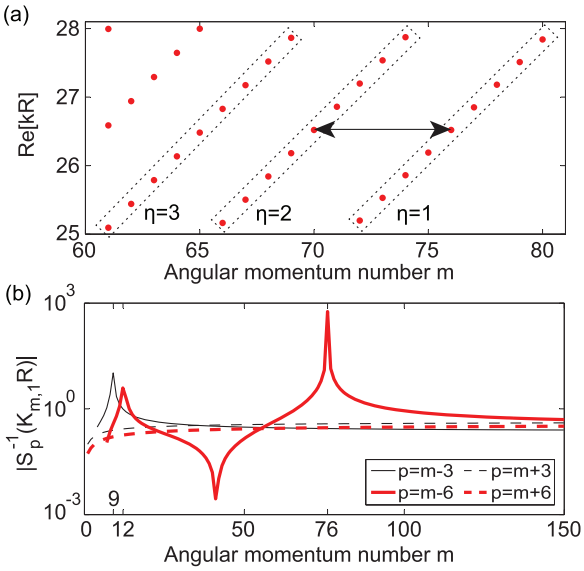

FIG. 10. (Color online) (a) TM spectrum of a circular cavity with refractive index $n = 3.13$ near $\mathrm{Re}[KR] = 27$. Dashed boxes indicate the first three bands with radial quantum number $\eta = 1,2,3$. $K_{m=76,\eta=1}$ and $K_{m=70,\eta=2}$ are marked by the horizontal arrows. They are the closest quasidegenerate pair in the frequency range. (b) Spectral function $|S_{m\pm\nu}^{-1}(K_{m,1}R)|$ for the first-order scattering $m \to m \pm \nu$ as a function of m for $\nu = 3$ and 6. The peak of $S_{m-6}^{-1}(K_{m,1}R)$ at $m = 76$ is due to the quasidegeneracy shown in (a). Its other peak at $m = 12$ is due to another pair of quasidegenerate modes $K_{12,1}$ and $K_{6,3}$. The single peak of $S_{m-3}^{-1}(K_{m,1}R)$ at $m = 9$ is due to the quasidegeneracy between $K_{9,1}$ and $K_{6,2}$.

eventually becomes comparable to the small $S^{-1}_{m+\nu}(K_{m,1}R)$ we have discussed since now $K_{m-\nu,1}$ is the closest resonance of angular momentum $m-\nu$ to $K_{m,1}$ and $\Delta_{m,m-\nu} \approx \nu/n$, just as $K_{m+\nu,1}$ is the closest resonance of angular momentum $m+\nu$ to $K_{m,1}$ and $\Delta_{m,m+\nu} \approx \nu/n$.

Equation (A5) explains why the sensitivity of the high-Q modes of $\eta = 1$ on a low-order harmonic boundary deformation maximizes in the mesoscopic regime and becomes weak in the semiclassical limit. We note that quasidegeneracy also occurs among modes of much larger η's, such as the TM resonances $K_{50,10} = 30.187 - 9.6157 \times 10^{-6}i$ and $K_{47,11} = 30.186 - 9.6122 \times 10^{-6}i$ in a circular cavity of $n = 3.13$. We do not study them here because their relatively low quality factors make them difficult to observe experimentally. Their coupling, nevertheless, gives an alternative explanation to the contrasting intracavity and far-field intensity patterns found in Ref. [46], similar to what we have shown in Figs. 4 and 7.

[1] *Optical Processes in Microcavities*, edited by R. K. Chang and A. J. Campillo, Advanced Series in Applied Physics (World Scientific, Singapore, 1996).

[2] *Optical Microcavities*, edited by K. J. Vahala, Advanced Series in Applied Physics (World Scientific, Singapore, 2004).

[3] A. F. J. Levi, R. E. Slusher, S. L. McCall, T. Tanbun-Ek, D. L. Coblentz, and S. J. Pearton, IEEE Trans. Electron Devices **39**, 2651 (1992).

[4] S. L. McCall, A. F. J. Levi, R. E. Slusher, S. J. Pearton, and R. A. Logan, Appl. Phys. Lett. **60**, 289 (1992).

[5] H.-G. Park, S.-H. Kim, S.-H. Kwon, Y.-G. Ju, J.-K. Yang, J.-H. Baek, S.-B. Kim, and Y.-H. Lee, Science **305**, 1444 (2004).

[6] J. U. Nöckel and A. D. Stone, Nature (London) **385**, 45 (1997).

[7] C. Gmachl, F. Capasso, E. E. Narimanov, J. U. Nöckel, A. D. Stone, J. Faist, D. L. Sivco, and A. Y. Cho, Science **280**, 1556 (1998).

[8] A. Badolato, K. Hennessy, M. Atatüre, J. Dreiser, P. M. Petroff, and A. Imamoglu, Science **308**, 1158 (2005).

[9] E. Peter, P. Senellart, D. Martrou, A. Lemaître, J. Hours, J. M. Gérard, and J. Bloch, Phys. Rev. Lett. **95**, 067401 (2005).

[10] H. E. Türeci, H. G. L. Schwefel, Ph. Jacquod, and A. D. Stone, Prog. Opt. **47**, 75 (2005).

[11] J. Wiersig and M. Hentschel, Phys. Rev. Lett. **100**, 033901 (2008).

[12] Q. J. Wang *et al.*, Proc. Natl. Acad. Sci. USA **107**, 22407 (2010).

[13] Q. H. Song, L. Ge, A. D. Stone, H. Cao, J. Wiersig, J.-B. Shim, J. Unterhinninghofen, W. Fang, and G. S. Solomon, Phys. Rev. Lett. **105**, 103902 (2010).

[14] B. Redding, L. Ge, Q. Song, J. Wiersig, G. S. Solomon, and H. Cao, Phys. Rev. Lett. **108**, 253902 (2012).

[15] W. D. Heiss, Phys. Rev. E **61**, 929 (2000).

[16] Y. Wu, Phys. Rev. A **54**, 4534 (1996).

[17] H. E. Türeci, L. Ge, S. Rotter, and A. D. Stone, Science **320**, 643 (2008).

[18] A. W. Snyder and J. D. Love, *Optical Waveguide Theory* (Chapman and Hall, London, 1991).

[19] J. Wiersig and M. Hentschel, Phys. Rev. A **73**, 031802(R) (2006).

[20] J. Wiersig, Phys. Rev. Lett. **97**, 253901 (2006).

[21] L. Ge, Q. H. Song, B. Redding, and H. Cao, Phys. Rev. A **87**, 023833 (2013).

[22] E. Pérez, Math. Models Methods Appl. Sci. **13**, 75 (2003).

[23] F. Manni, K. G. Lagoudakis, T. C. H. Liew, R. André, and B. Deveaud-Plédran, Phys. Rev. Lett. **107**, 106401 (2011).

[24] M. A. Reed, J. N. Randall, R. J. Aggarwal, R. J. Matyi, T. M. Moore, and A. E. Wetsel, Phys. Rev. Lett. **60**, 535 (1988).

[25] R. Dubertrand, E. Bogomolny, N. Djellali, M. Lebental, and C. Schmit, Phys. Rev. A **77**, 013804 (2008).

[26] J. Wiersig, Phys. Rev. A **85**, 063838 (2012).

[27] E. E. Narimanov, G. Hackenbroich, P. Jacquod, and A. D. Stone, Phys. Rev. Lett. **83**, 4991 (1999).

[28] Q. Song, L. Ge, B. Redding, and H. Cao, Phys. Rev. Lett. **108**, 243902 (2012).

[29] F. G. Bass and I. M. Fuks, *Wave Scattering from Statistically Rough Surfaces* (Pergamon, Oxford, 1979).

[30] J. A. Ogilvy, *Theory of Wave Scattering from Random Rough Surfaces* (Hilger, Bristol, UK, 1991).

[31] J. M. Bennett and L. Mattsson, *Introduction to Surface Roughness and Scattering*, 2nd ed. (Optical Society of America, Washington, DC, 1999).

[32] P. Roberts, F. Couny, H. Sabert, B. Mangan, T. Birks, J. Knight, and P. Russell, Opt. Express **13**, 7779 (2005).

[33] F. M. Izrailev, N. M. Makarov, and M. Rendón, Phys. Rev. B **72**, 041403(R) (2005).

[34] G. B. Akguc and J. Gong, Phys. Rev. B **78**, 115317 (2008).

[35] D. Dominé, F.-J. Haug, C. Battaglia, and C. Ballif, J. Appl. Phys. **107**, 044504 (2010).

[36] S. Schröder, A. Duparré, L. Coriand, A. Tünnermann, D. H. Penalver, and J. E. Harvey, Opt. Express **19**, 9820 (2011).

[37] J.-B. Shim, S.-B. Lee, S. W. Kim, S.-Y. Lee, J. Yang, S. Moon, J.-H. Lee, and K. An, Phys. Rev. Lett. **100**, 174102 (2008).

[38] F. D. M. Haldane and S. Raghu, Phys. Rev. Lett. **100**, 013904 (2008).

[39] Z. Wang, Y. D. Chong, J. D. Joannopoulos, and M. Soljacic, Nature (London) **461**, 772 (2009).

[40] M. C. Rechtsman *et al.*, Nature (London) **496**, 196 (2013).

[41] Y. R. Shen, *The Principles of Nonlinear Optics* (Wiley, New York, 1984).

[42] G. Bahl, M. Tomes, F. Marquardt, and T. Carmon, Nat. Phys. **8**, 203 (2012).

[43] X. Cai *et al.*, Science **338**, 363 (2012).

[44] S. E. Harris, Phys. Today **50**(7), 36 (1997).

[45] J. U. Nöckel, Ph.D. thesis, Yale University, 1997.

[46] S. C. Creagh and M. M. White, Phys. Rev. E **85**, 015201(R) (2012).